Optical properties of GaNAs and GaInAsN quantum wells

2004 J. Phys.: Condens. Matter 16 S3387

(http://iopscience.iop.org/0953-8984/16/31/026)

INSTITUTE OF PHYSICS PUBLISHING JOURNAL OF PHYSICS: CONDENSED MATTER

J. Phys.: Condens. Matter **16** (2004) S3387–S3412 PII: S0953-8984(04)75322-9

Optical properties of GaNAs and GaInAsN quantum wells

R J Potter[1,2] **and N Balkan**[1]

[1] Photonics Group, Department of ESE, University of Essex, Colchester CO4 3SQ, UK
[2] Material Science and Engineering, University of Liverpool, Ashton Building, Liverpool L69 3BX, UK

Received 22 January 2004
Published 23 July 2004
Online at stacks.iop.org/JPhysCM/16/S3387
doi:10.1088/0953-8984/16/31/026

Abstract

We present an overview of our optical characterization work on dilute nitride quantum well (QW) samples. A simple model for calculating interband transition energies is constructed, tested against published $\boldsymbol{k} \cdot \boldsymbol{p}$ results and used to model experimental data. Steady state photoluminescence (PL), time-resolved PL and photomodulated reflectance measurements are utilized to characterize GaNAs/GaAs, GaInNAs/GaAs and InGaAs/GaAs QWs. The effects of carrier localization, hot-carrier relaxation, non-radiative recombination and the reduced bandgap temperature dependence of dilute nitrides are investigated. Emission from recombining hot carriers in a GaInNAs/GaAs QW is recorded and used to estimate the LO-phonon scattering energy. The addition of small fractions of N is found to have little effect on phonon energy, which is found to be $\hbar\omega = 29.7$ meV.

(Some figures in this article are in colour only in the electronic version)

1. Introduction

The low loss window of optical fibres now extends from around 1.26 to 1.68 μm [1, 2], potentially offering huge optical network capacities. As a result, optoelectronic devices (such as lasers, detectors, filters and optical amplifiers) operating in this wavelength range dominate current photonics research. Much of this research is concerned with enhancing device performance, increasing reliability and lowering final system costs. The performance of many photonic devices has recently been enhanced using distributed Bragg reflectors (DBRs) to control the optical field. Typical examples include vertical cavity surface emitting lasers (VCSELs) [3–5], resonant cavity enhanced (RCE) photodetectors [6, 7], RCE-LEDs [8] and vertical cavity semiconductor optical amplifiers (VCSOA) [9]. Unfortunately, the requirements of such devices are not met by conventional optoelectronic materials such as InGaAs/GaAs or InGaAsP/InP.

Conventional GaAs-based materials are very attractive for optoelectronics: however, systems like InGaAs/GaAs only allow device operation out to about 1.2 μm [10]. In contrast, InP-based devices can easily operate within the desired wavelength window: however, they suffer from poor thermal stability (lowering efficiency) [11] and low refractive index contrast (hindering DBR fabrication). Many layers are therefore required to produce high-reflectivity InP-based DBRs, presenting large growth challenges as well as introducing high series resistance, which retards device dynamics. Various solutions to these problems have been investigated, including wafer fusing of AlGaAs/AlAs DBRs to the active layers. However, this complicates fabrication, increasing cost and may result in unreliable devices [12, 13].

Dilute nitrides avoid many of the problems associated with conventional arsenides and phosphides. Incorporating a few per cent of nitrogen into (In)GaAs has a profound influence on its electronic properties. In most III–V materials, substituting an element for one with a smaller atomic radius reduces the lattice constant and increases the bandgap. However, Weyers *et al* found that replacing a fraction of arsenic atoms in GaAs with smaller N atoms rapidly reduces the bandgap [14]. In addition, nitrogen allows band alignment, lattice constant and strain to be tailored, opening up a new dimension of band engineering [15]. The quaternary alloy GaInNAs is particularly attractive for a range of devices, offering several advantages over conventional narrow-gap materials. GaInNAs quantum wells (QWs) can be grown pseudomorphically on GaAs, giving strong carrier confinement (hence thermal stability) [11], compatibility with GaAs technology (including AlGaAs/AlAs DBRs), extensive control of bandgap energy, strain and band alignment. GaNAs is less attractive for device applications: however, it allows investigation into the physical properties of dilute nitrides.

A wide range of novel devices may benefit from dilute nitride technology. In fact, GaInNAs-based VCSELs [3–5], VCSOAs [9], RCE-photodetectors [6, 7], RCE-LEDs [8], multijunction solar cells [16–18], modulators [19] and heterojunction bipolar transistors (HBTs) [20–22] have already been demonstrated. Commercially, the most important devices are for inexpensive 1.3 μm metro-area (10–20 km) optical fibre data transmission links [15]. These links are presently considered to be the bottleneck for large-scale optical communications and constitute a very large market volume. Rapid progress has already led to the demonstration of high quality 1.3 μm dilute nitride laser diodes [23–26] and VCSELs [27]. Emission from dilute nitride devices has even been pushed above 1.5 μm [28, 29], potentially useful for long haul links.

In this work, we investigate the optical properties of GaNAs/GaAs, GaInNAs/GaAs and InGaAs/GaAs QWs using steady-state photoluminescence (PL), time-resolved PL and photomodulated reflectance (PR) measurements. The results are modelled using a parabolic band approach, with the effect of nitrogen accounted for via the band-anticrossing (BAC) method [30]. We describe the model, test it against published $\boldsymbol{k}\cdot\boldsymbol{p}$ model results and show that calculated interband transitions compare well with experimental data. We discuss the effects of carrier localization, which is common in dilute nitrides, and the reduction in bandgap temperature dependence, which is intrinsic. We also discuss non-radiative recombination, which often limits the optical quality of dilute nitrides. Finally, we investigate the relaxation of non-equilibrium carriers after optical excitation, which is dominated by optical phonon scattering.

2. Experimental details

Quantum well (QW) samples (table 1) were deposited on semi-insulating (100) GaAs substrates by solid source MBE in a RIBER-32 chamber. Growth temperatures of 580–600 °C were used during GaAs deposition and 400–500 °C during Ga(In)NAs deposition. Reactive N was

Table 1. Details of samples investigated in this work, including estimates of composition.

Sample no.	Structure	Well width (nm)	$Ga_xIn_{1-x}N_yAs_{1-y}$		Growth notes		
			x	y	N flow (sccm)	RF power (W)	V/III gas phase ratio
752	DQW	9	0.8	0.015	0.01	200	5
933	SQW Optical laser	9	0.8	0.015	0.015	180	3.5
960	TQW	6	0.75	0			5.5
				0.01	0.002	110	
				0.018	0.01	200	
961	TQW	6	0.8	0			5.5
				0.01	0.002	110	
				0.018	0.01	200	
962	TQW	6	0.7	0			5.5
				0.01	0.002	110	
				0.018	0.01	200	
983	DQW	6	0.7	0			8
				0.01	0.002	110	
994	GaNAs SQW	8.2	1	0.08	0.002	110	8
996	GaNAs SQW	8.2	1	0.0225	0.01	200	8
997	GaNAs SQW	8.2	1	0.018	0.01	150	8
998	GaNAs SQW	8.2	1	0.028	0.01	300	8
1082	DQW	6.5	0.7–0.6	0.015	0.01	200	4
1087a	DQW (annealed)	6	0.7	0.015	0.01	200	4
1087b	DQW	6	0.7	0.015	0.01	200	4

generated by a RF atom source (operated at 13.56 MHz) and was 'leaked' into the MBE chamber during dilute nitride deposition. Figure 1 shows a bright field TEM image of a typical double QW (DQW) structure with an InGaAs lower well and GaInNAs upper well.

Steady state PL measurements were carried out between ∼2 K and room temperature (RT) using the 647.1 nm line of a krypton-ion laser. The beam was mechanically chopped and focused to defining a ∼250 μm diameter spot on the sample. The luminescence was spectrally dispersed by a 1/3 m Czerny–Turner monochromator and detected using a cooled InP/InGaAs photomultiplier in conjunction with a boxcar averager.

For time resolved PL (figure 2), the samples were excited with 1.4 ps pulses (82 MHz repetition rate) from a mode locked Ti–sapphire laser tuned to 800 nm (1.55 eV). This was focused to define a 200 μm diameter spot on the sample. Pump intensity was controlled using a variable neutral density filter (ND2) and sample temperature using a closed cycle cryostat. The luminescence was spectrally dispersed by a 1/3 m monochromator and temporally resolved by a 2D streak camera. This was synchronized with the laser using synchroscan sweep and

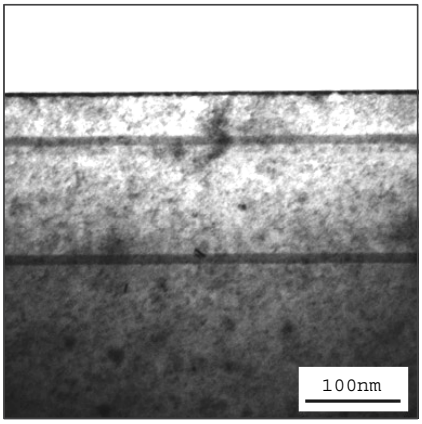

Figure 1. Bright field TEM of sample no. 752: a double QW structure, with InGaAs (lower) and GaInNAs (upper) wells.

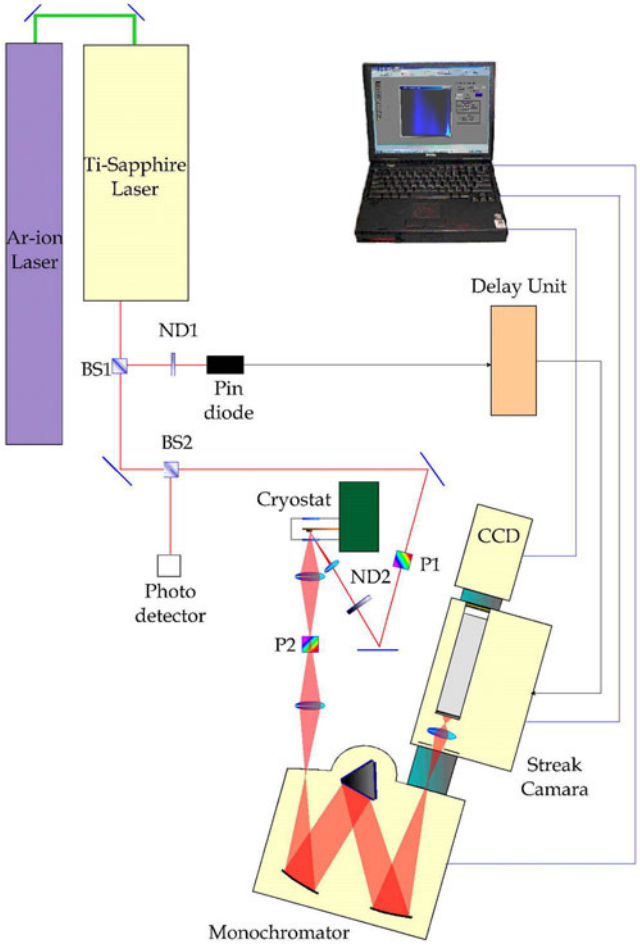

Figure 2. Time-resolved PL set-up, where BS1 and BS2 are beamsplitters, ND1 is a neutral density filter, ND2 is a variable neutral density filter used to adjust pump power and P1 and P2 are polarizers.

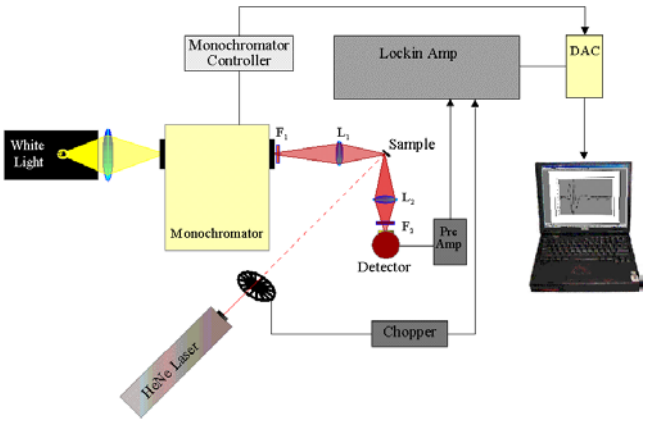

Figure 3. Photomodulated reflectance experimental set-up, where F_1 and F_2 are long pass filters and L1 and L2 are lenses.

delay units triggered by a pin diode. The output from the streak camera was recorded using a CCD camera connected to a PC. Results were calibrated prior to analysis to compensate for the S1 photocathode spectral response.

Photomodulated reflectance (PR) measurements were carried out using a conventional pump probe technique (figure 3). A halogen lamp in conjunction with a 1/3 m monochromator and long pass filter was used to generate the probe beam. This was focused onto the sample at ∼45° and the reflected beam focused onto a cooled Ge photodiode. The pump beam from an optically chopped (∼300 Hz) 633 nm HeNe laser was focused onto the sample (at near normal incidence), overlapping the probe beam. The AC component (ΔR) of the collected signal was recovered and radioed with the DC component (R) using a lock-in amplifier. $R/\Delta R$ was measured as a function of the probe beam wavelength.

3. Model

The effect of nitrogen on the band structure of Ga(In)NAs has recently been explained using the band anti-crossing (BAC) approach [30]. This has been widely adopted in conjunction with $\boldsymbol{k}\cdot\boldsymbol{p}$ modelling to calculate the band structure of dilute nitrides close to $\boldsymbol{k}=0$. While the $\boldsymbol{k}\cdot\boldsymbol{p}$ approach is powerful, allowing for interband interaction and hence non-parabolicity of bands, it is computationally demanding and does not favour intuitive estimations. A much simpler approach is to assume that the bands are parabolic. It is well established that strain-induced band repulsion helps to restore parabolicity (figure 4 [31]) and, although GaInNAs can be lattice matched to GaAs, it is often desirable to incorporate strain. We therefore, investigate the reliability of assuming parabolic bands when modelling interband transitions in strained Ga(In)NAs QWs. In this section, we outline the construction our model, test it against published $\boldsymbol{k}\cdot\boldsymbol{p}$ model results and compare calculated and experimental results.

In our model, the alignment between Ga(In)NAs and GaAs bands was estimated using model solid theory [32] incorporating strain but not the direct effect of nitrogen (incorporated later). Applying this to both cladding and well materials gives the relative energies of the bands on an 'absolute' scale and hence the band alignments. Expressions for the heavy-hole (hh), light-hole (lh) and conduction (c) energy levels are given in equations (1)–(3) respectively:

$$E_{\mathrm{hh}} = E_{\mathrm{v,av}} + \frac{\Delta_{\mathrm{SO}}}{3} + \Delta E_{\mathrm{hh}} \tag{1}$$

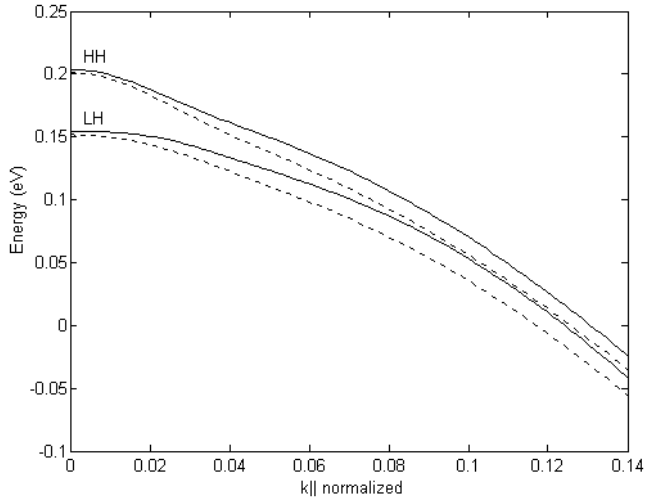

Figure 4. Valence band structure of GaInNAs QWs designed for 1.3 μm emission calculated using $\boldsymbol{k}\cdot\boldsymbol{p}$ theory, illustrating the parabolicity of the bands due to strain. (——) $Ga_{0.733}In_{0.267}N_{0.033}As_{0.967}$ $\sim -1.24\%$ strain and (– – –) $Ga_{0.667}In_{0.333}N_{0.025}As_{0.976}$ $\sim 1.85\%$ strain [31].

$$E_{\mathrm{lh}} = E_{\mathrm{v,av}} + \frac{\Delta_{\mathrm{SO}}}{3} + \Delta E_{\mathrm{lh}} \tag{2}$$

$$E_{\mathrm{C}} = E_{\mathrm{v,av}} + \frac{\Delta_{\mathrm{SO}}}{3} + E_{\mathrm{g}} + \Delta E_{\mathrm{e}} \tag{3}$$

where $E_{\mathrm{v,av}}$ is the average energy of the three top valence bands (hh, lh and SO bands) obtained from full self-consistent calculations ($E_{\mathrm{v,av}}$ values obtained from [32]), Δ_{SO} is the spin–orbit split-off energy, E_{g} is the bandgap energy and ΔE_{hh}, ΔE_{lh} and ΔE_{e} are the band edge shifts due to the strain for the hh, lh and conduction band, respectively, given by equations (4)–(6) [33]:

$$\Delta E_{\mathrm{hh}} = -P_{\mathrm{v}} - Q \tag{4}$$

$$\Delta E_{\mathrm{lh}} = -P_{\mathrm{v}} + \tfrac{1}{2}\left(Q - \Delta_{\mathrm{SO}} + \sqrt{\Delta_{\mathrm{SO}}^2 + 2\Delta_{\mathrm{SO}}Q + 9Q^2}\right) \tag{5}$$

$$\Delta E_{\mathrm{e}} = -P_{\mathrm{c}} \tag{6}$$

where

$$P_{\mathrm{c}} = -2a_{\mathrm{c}}\frac{C_{11}-C_{12}}{C_{11}}\varepsilon, \qquad P_{\mathrm{v}} = 2a_{\mathrm{v}}\frac{C_{11}-C_{12}}{C_{11}}\varepsilon,$$

$$Q = -b\frac{C_{11}+2C_{12}}{C_{11}}\varepsilon \qquad \text{and} \qquad \varepsilon = \frac{a_{\mathrm{s}}-a_{\mathrm{w}}}{a_{\mathrm{w}}}$$

where a_{s} and a_{w} are substrate and QW lattice constants, C_{11} and C_{12} are in-plane and out-of-plane elastic stiffness constants, a_{c} and a_{v} are hydrostatic deformation potentials for conduction and valence bands and b is the shear deformation potential. The strain related parameters for GaInNAs were estimated using Vegard's law or quadratic equations [34].

Nitrogen is known to primarily affect the conduction band, resulting in improved electron confinement in Ga(In)NAs QWs. However, its effect on the valence band is not fully established, with some studies suggesting reduced hole confinement [35–37], while others indicate an increase [38–43]. Several published $\boldsymbol{k}\cdot\boldsymbol{p}$ [31, 42] and tight-binding [39, 44] models use band alignment as a fitting parameter, hence we adopt a similar approach. The conduction

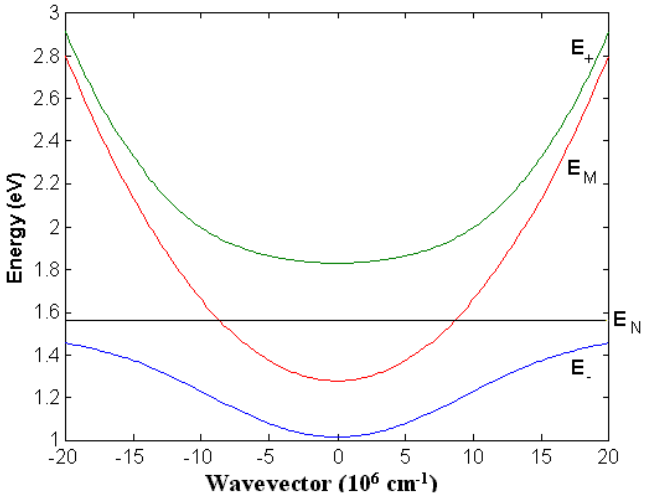

Figure 5. *E–k* diagram of the dilute nitride band structure calculated using the BAC approach.

and valence bands are shifted by αy and χy, respectively, where α and χ are constants and y is the nitrogen fraction.

The alignment of the localized N level E_N in GaAs has been modelled using tight-binding calculations [39, 44]. At very low nitrogen fractions the wavefunctions of individual N atoms do not significantly overlap, hence they act as isoelectric impurities with energy E_N^0 (∼1.7 eV) [42, 44]. However, as the nitrogen fraction increases (above ∼0.2%) [45] wavefunctions start overlapping, forming a resonant energy band E_N. The energy of this relative to the valence band of GaAs is given by equation (7). As with many highly localized centres, the nitrogen level is not affected by the surrounding lattice. It therefore remains at the same energy relative to the vacuum level in InGaAs as in GaAs [46, 47]. Hence, the relative positions of the highly localized N state (E_N) and the extended conduction band (E_M) are simply found from the band alignment:

$$E_N = E_N^0 - \gamma y. \tag{7}$$

The interaction between E_N and E_M is determined using perturbation theory, leading to the BAC eigenvalue equation (equation (8)) [30]. The dilute nitride conduction band dispersion relations is given by solutions to this eigenequation of the form given in equation (9). In this the extended E_M band is assumed parabolic (equation (10)), with a minimum at $k = 0$ and the interaction between E_N and E_M is described by the matrix element V_{MN} (equation (11), in which C_{MN} is a constant) [44]. Hence the dispersion curves can be calculated by combining equations (9) and (10) for a range of k values. This gives two possible solutions, manifested as a splitting of the conduction band into two distinct bands (E_+ and E_-). The E_- band is pushed downwards relative to E_M, while E_+ is pushed upwards (figure 5). It is assumed that E_N does not couple with the valence bands [42, 48]:

$$\begin{vmatrix} E - E_M & V_{MN} \\ V_{MN} & E - E_N \end{vmatrix} = 0 \tag{8}$$

$$E_\pm(k) = \frac{E_N + E_M(k) \pm \sqrt{(E_N - E_M(k))^2 + 4V_{MN}^2}}{2} \tag{9}$$

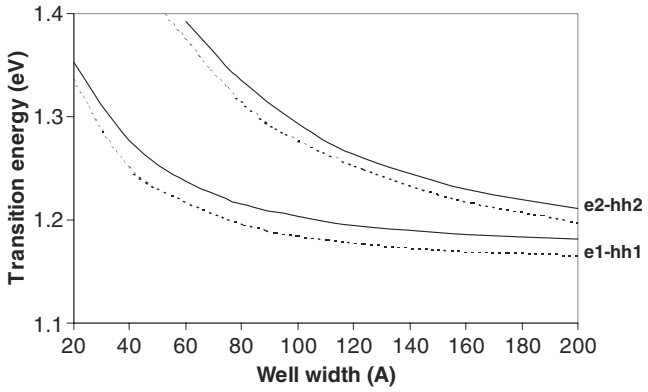

Figure 6. Well width dependence of inter-band transitions in GaNAs with 1.8% nitrogen, as modelled using the current model (full lines) and $\boldsymbol{k}\cdot\boldsymbol{p}$ model (dotted lines) reported in [42].

$$E_{\mathrm{M}}(k) = E_{\mathrm{M}}(0) + \frac{\hbar^2 k^2}{2m^*} \tag{10}$$

where k is the wavevector and m^* is the electron effective mass of the InGaAs:

$$V_{\mathrm{MN}} = -C_{\mathrm{MN}}\sqrt{y}. \tag{11}$$

The standard density-of-states effective mass definition and the dispersion relations was used to estimate the electron effective mass (equation (12) [49], where E is the electron energy and m^*(InGaAs) is the electron effective mass in (In)GaAs). We assume that nitrogen has little effect on hole effective masses and therefore calculate values from the Luttinger parameters of (In)GaAs [33, 34]. Finally, the quantum confined electron and hole energy levels, and hence interband transition energies, were calculated using a standard numerical finite square well approach [33]:

$$m^*(E) = m^*(\mathrm{GaInAs})\left[1 + \left(\frac{V_{\mathrm{MN}}}{E_{\mathrm{N}} - E}\right)^2\right]. \tag{12}$$

The bandgap pressure and temperature dependence of (In)GaAs is significantly reduced by the addition of nitrogen [50–53]. This behaviour can be explained and quantified using the model [51]. Localized impurity-like states are known to be almost independent of pressure or temperature. The temperature (or pressure) dependence of Ga(In)NAs can therefore be modelled by assuming that E_{N} remains constant while E_{M} following the temperature (or pressure) dependence of (In)GaAs. In this work the temperature dependence of E_{M} was obtained from both experimental measurements of (In)GaAs emission [54] and analytical expressions. In the latter case, the temperature dependence of GaAs and InAs are found using the Varshni [34, 55] or four-parameter (4P) [56] expressions and the bowing [34] approach used to find the dependence of InGaAs.

3.1. Model testing

To test the model, results from it were compared with published $\boldsymbol{k}\cdot\boldsymbol{p}$ data, using the published model parameters in our calculations. Figure 6 shows the e1–hh1 and e2–hh2 transitions of a GaNAs QW as a function of well width. While our results are slightly blue shifted compared to the $\boldsymbol{k}\cdot\boldsymbol{p}$ data (taken from [42]), the overall agreement is good. Figure 7 shows compositions of GaInNAs required QW emission at 1.3 μm. Again the agreement between our results and those reported in [31] is good.

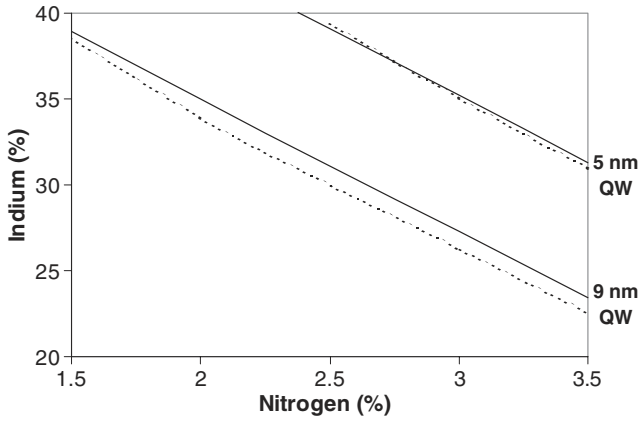

Figure 7. Composition required for 1.3 μm emission in GaInNAs/GaAs QWs as modelled using the current model (full lines) and $\boldsymbol{k} \cdot \boldsymbol{p}$ model (dotted lines) reported in [31].

Table 2. Published band anti-crossing (BAC) model parameters.

Parameter	[42]	[44]
$E_N = E_N^0 - \gamma y$	$1.7 + 3.89y$	$1.675 - 2.52y$
α	1.55	1.55
χ	3.88	0.2
C_{MN}	2.4	1.5

3.2. Model parameters

While testing our model, we used the model-specific parameters given in the associated $\boldsymbol{k} \cdot \boldsymbol{p}$ literature, so in this section we will discuss these parameters further. The γ, α and χ parameters govern the effect of nitrogen on the N state, conduction band edge and valence band edge, respectively. Values of these have been determined using a combination of tight binding calculations [39, 44] and experimental fitting [42, 44] (table 2). However, there are significant discrepancies between reported values of γ. For example, γ is positive in [42], implying that the N state shifts to higher energies with increasing nitrogen, while in [44] it is negative, implying the opposite. These parameters will be discussed later in light of our experimental results.

It has been suggested that C_{MN} (sometimes denoted β) is independent of composition [51]. While this is supported by some experimental observations [49, 57], other studies indicate an indium dependence [30, 44, 54, 58]. Physically it is reasonable to assume that the value of C_{MN} will have an indium dependence as it affects the overlap, and hence the interaction strength, of E_M and E_N. However, published values of C_{MN} (table 3) are found to vary considerably even at a fixed indium concentration. This may originate from a number of experimental and modelling sources, such as errors in nitrogen fraction measurements, different model approaches, choice of parameters or nearest-neighbour (NN) environment of nitrogen atoms in GaInNAs [31].

Recent work using tight binding calculations [59] suggests that each nitrogen site may be surrounded by one of five NN configurations; four gallium atoms (4Ga), three gallium plus one indium (3Ga), and so on, up to four indium atoms (0Ga). During MOCVD of GaInNAs, Ga–N bonds are favoured; hence Ga-rich NN configurations are preferred. However, indium-rich NN configurations are energetically favoured in the lattice: therefore, with appropriate

Table 3. Published values for the interaction matrix element constant C_{MN}.

Indium fraction	C_{MN} (or β)	References
0	1.5	[44]
0	2.03	[58]
0	2.5	[51]
0	2.7	[49]
4	2.7	[57]
5	1.83	[30]
8	2.5	[51]
8	2.64	[30]
0	2.4	[42]
20	3.2 ± 0.25	[54]

annealing conditions the structure undergoes a phase change. This transformation causes an increase in the bandgap, in keeping with the emission blueshift commonly observed after annealing. The NN environments can have a significant effect on the bandgap, with a maximum energy difference of more than 100 meV between 4Ga and 0Ga environments [59]. Additional experimental [60] and theoretical work based on Monte Carlo simulation [61] supports the NN interpretation. If the effects of NN environment on bandgap is accounted for via the C_{MN} parameter, then a single composition can give five different C_{MN} parameters [31].

4. Experimental results

4.1. Localized exciton recombination

PL emission from high quality quantum well and bulk samples is typically characterized by symmetric, Gaussian-like, features; this is illustrated for InGaAs and GaAs in figures 8(b) and (d), respectively. However, emission from dilute nitride samples is often characterized by asymmetric peaks (figures 8(a) and (c)) with low-energy exponential tails [62–67]. These tail states originate from recombination of localized excitons trapped in potential fluctuations. The localized exciton density of states can be described by equation (13), where Δ is the approximate localization potential [68]. Hence, from the low energy tails we can estimate the localization potentials (table 4). If the localization is attributed solely to interface roughness then well width fluctuations can be estimated. For sample no. 725 the localization corresponds to $\Delta L \sim 2$ and 3–4 monolayers for the InGaAs and GaInNAs wells, respectively, while for the GaNAs well of no. 994 $\Delta L \sim 6$–7 monolayers. TEM images (such as figure 1) confirm the existence of small width fluctuations: however, it is likely that compositional fluctuations and different NN configurations also contribute to the observed localization:

$$\rho(E) \propto \mathrm{e}^{E/\Delta}. \tag{13}$$

The effects of localization are also evident in the peak emission energy (figure 9) and spectral width (figure 10) temperature dependence. In the low-temperature region (typically $<$100 K), there is a clear S-shape (redshift–blueshift–redshift) behaviour in the peak. Between 0 K and the redshift minima, excitons thermalize into the lowest available energy states. As the temperature increases further, trapped excitons, first in shallow and then deeper potentials, acquire sufficient thermal energy to allow de-trapping. This results in a blueshift of the peak as tail state emission is suppressed. Finally, all excitons become delocalized, the tail emission dies and the peak follows the normal bandgap temperature dependence. This behaviour is well

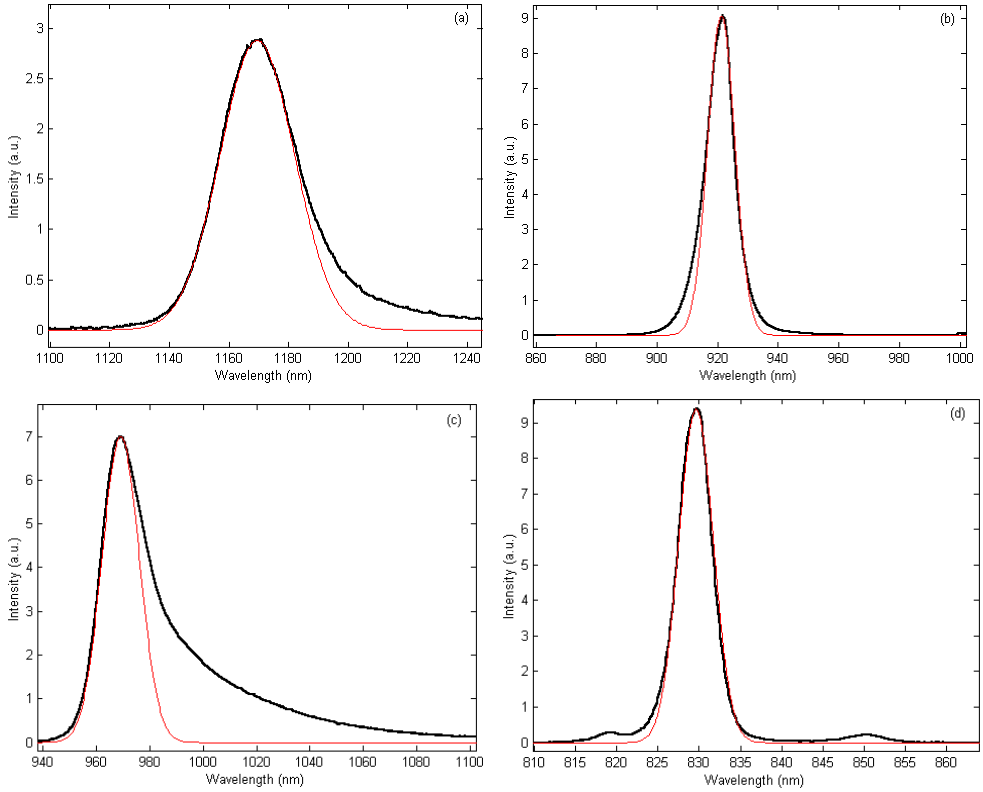

Figure 8. Low temperature (10 K) spectral emission peaks (thick curves), overlaid with Gaussian curves (thin curves). (a) No. 752 GaInNAs, (b) no. 752 InGaAs, (c) no. 994 GaNAs and (d) no. 994 GaAs.

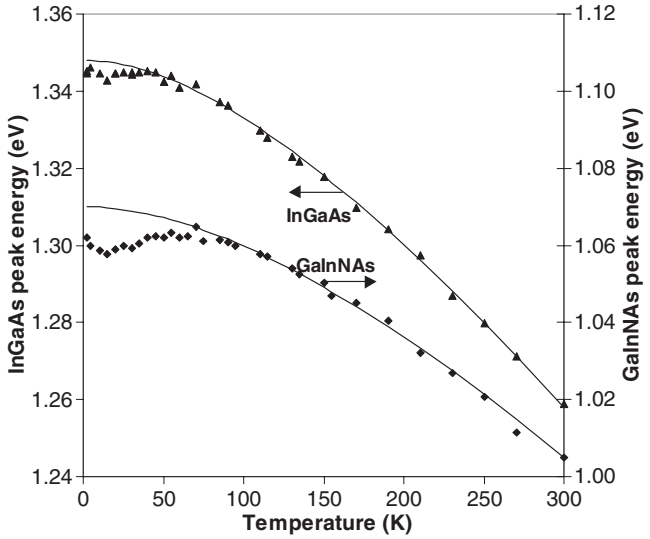

Figure 9. Peak emission energy temperature dependence of the InGaAs and GaInNAs QWs of sample no. 752 with fitted Varshni curves.

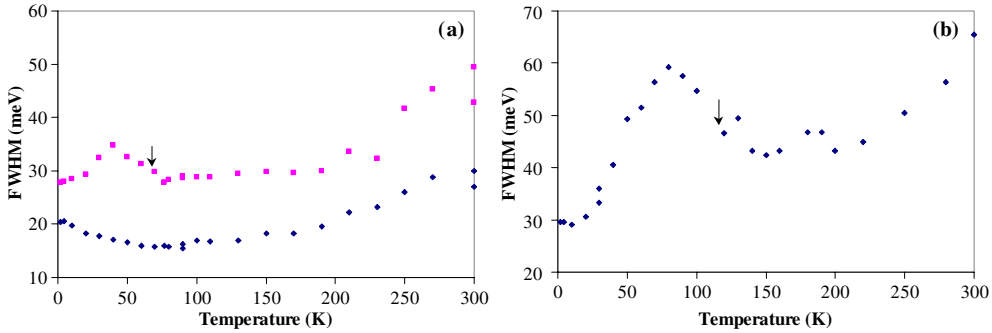

Figure 10. Temperature dependence of spectral width (fwhm). (a) Sample no. 983, where (♦) represent the InGaAs and (■) the GaInNAs peaks, and (b) GaNAs sample no. 994.

Table 4. Estimated localization potentials from emission lineshape (Δ) and S-shape temperature dependence (E_{Max}).

Sample no.	Quantum well	Δ (meV)	E_{10} (meV)	E_{Max} (meV)	T_{Max} (K)	T_{deloc} (K)
752	InGaAs	6.3	3	4	16	40
	GaInNAs	14.8	10	12	22	78
933	GaInNAs	15.5	6	8	30	64
960	InGaAs	4.1	1	3	27	40
	GaInNAs1	22.6	10	13	36	76
	GaInNAs2	39.5	7	9	30	72
961	InGaAs	3.1	0	0		
	GaInNAs1	26.6	12	14	36	92
	GaInNAs2	34	11	13	35	74
962	InGaAs	7.4	2	2	21	33
	GaInNAs1	49	18	21	50	98
	GaInNAs2	45.4				
983	InGaAs	12	1	2	20	33
	GaInNAs	17.0	7.5	9	26	69
994	Bulk GaAs		0	0		
	GaNAs	43.7	11.5	18	53	115
996	GaNAs	44.9	16.5	23	60	112
997	GaNAs	67.9	14.5	25	65	120
998	GaNAs	36.7	12	17	57	116

known for nitrides such as InGaN [69–72] and AlGaN [72], and is often seen in dilute nitride emission [62, 73–76].

In the absence of tail states, the spectral linewidth increases with temperature due to thermal broadening. This is observed for the InGaAs fwhm (figure 10(a)) for all but very low temperatures. However, the linewidth of our dilute nitride samples (figure 10(b)) broadens rapidly with temperature as the population of tail states increases, then narrows as de-trapping occurs and finally begins to broaden again in keeping with the expected thermalization of carriers.

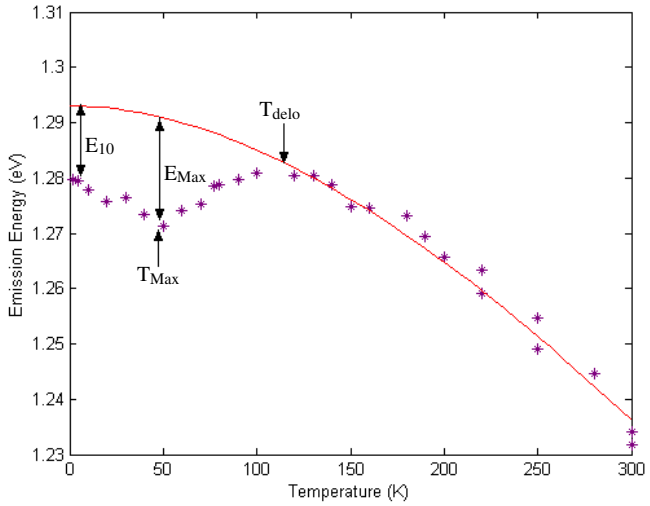

Figure 11. Diagram illustrating S-shape temperature-dependent measurements (sample no. 994).

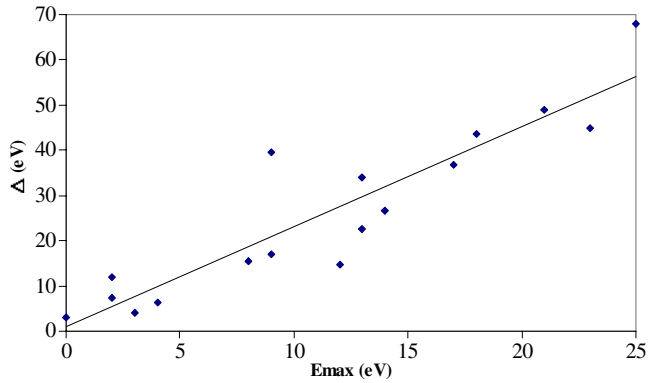

Figure 12. Correlation between S-shape maximum localization energies and the low energy tail localization energies.

To quantify the S-shape behaviour, we measure the mismatch between experimental data and fitted Varshni curves (figure 11). We measure the localization energies at ∼10 K (E_{10}) and at the redshift maximum (E_{Max}) together with the temperatures of maximum localization (T_{Max}) and delocalization (T_{deloc}) (table 4). As expected there is a strong correlation between E_{Max} and T_{deloc}, with increasing E_{Max} resulting in increased T_{deloc}. The measured E_{Max} values are also found to correlate closely with the Δ values found using the PL lineshapes (figure 12). However, the values found using the latter method are about double those found using the S-shape analysis. This discrepancy results from the indirect way in which the S-shape relates to the localization.

Low temperature (10 K) time resolved PL measurements are also affected by localization. The temporal evolution of the InGaAs (no. 752) emission peak does not shift significantly with time (figure 13(a)). In contrast, the GaInNAs emission from samples no. 752 (figure 13(b)) and no. 1087 (figure 14) is redshifted over time. For sample no. 752, the GaInNAs peak shifts by around 20 meV in the first 200 ps, converging towards the energy observed using steady state

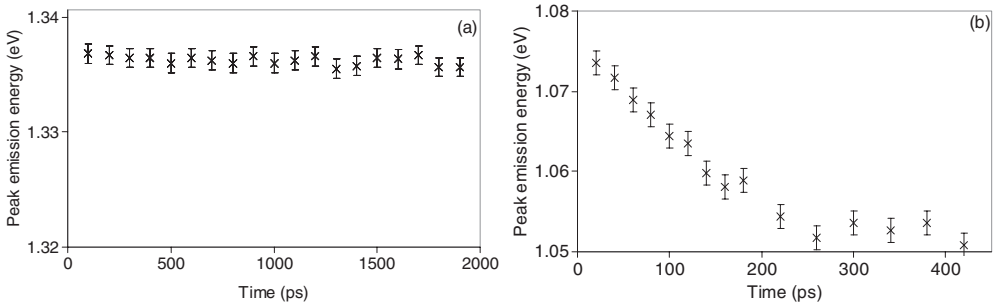

Figure 13. Peak emission energy versus time for sample no. 752 at 10 K with 5 mW pumping, (a) InGaAs peak and (b) GaInNAs peak.

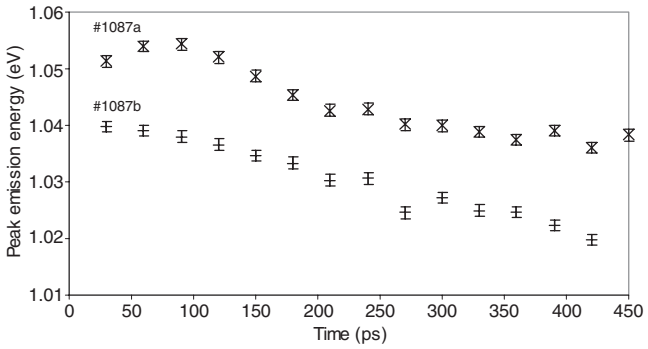

Figure 14. Peak emission energy versus time for sample no. 1087 at 10 K with 5 mW pumping for both annealed (no. 1087a) and un-annealed (no. 1087b) samples.

PL. This is close to the localization energy (Δ) calculated earlier. Similar for sample no. 1087, the GaInNAs peak shifts by around 15 meV in 250–300 ps after excitation. The observed shifts are due to carrier capturing into the localized states, which occurs on a sub-nanosecond timescale.

4.2. Reduced temperature dependence of bandgap energy

The effect of lattice temperature on the peak emission from GaNAs and GaInNAs wells are illustrated in figure 15 for samples nos. 994 and 752, respectively. For comparison, GaAs and InGaAs results are shifted to overlay the GaNAs and GaInNAs data, respectively. As previously discussed, the effects of localization dominate the low temperature peak behaviour. However, at higher temperatures (above ∼150 K) the peaks begin to decrease linearly as expected from the Varshni equation. The linear region slope is found to be much smaller for dilute nitride emission than for similar N-free samples. For the GaNAs of sample no. 994, the slope is ∼0.32 meV K^{-1}, which is ∼19% lower than the GaAs (∼0.4 meV K^{-1}). For the GaInNAs of sample no. 752, the slope is ∼0.3 meV K^{-1}, which is ∼27% lower than that measured for the InGaAs well (∼0.41 meV K^{-1}) in the same sample.

A strong correlation is found between RT emission energy and linear region slope of the GaNAs samples (figure 16), indicating that increasing nitrogen leads to a reduction in both emission energy and linear region temperature dependence. This behaviour can be explained using the BAC approach [30, 52, 77]. The interaction between the localized E_N level and

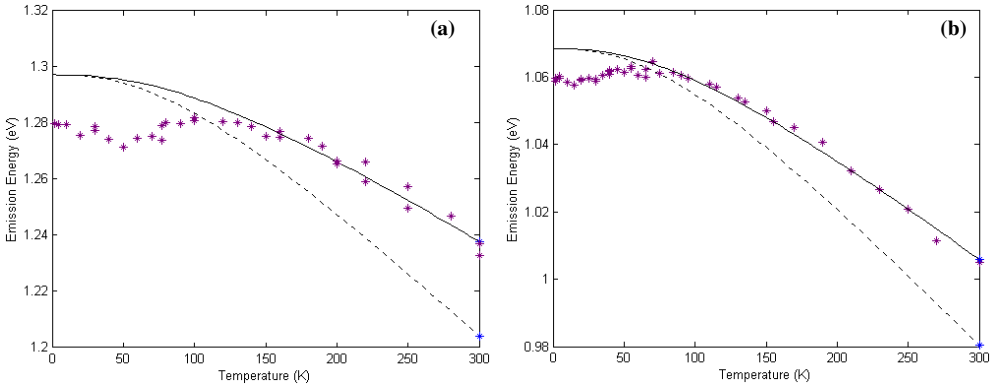

Figure 15. Bandgap temperature dependence (a) sample no. 994 GaNAs QW (∗) experimental data, (——) model fit and (– – –) shifted GaAs temperature dependence. (b) Sample no. 752 GaInNAs QW (∗) experimental data, (——) model fit and (– – –) shifted InGaAs temperature dependence.

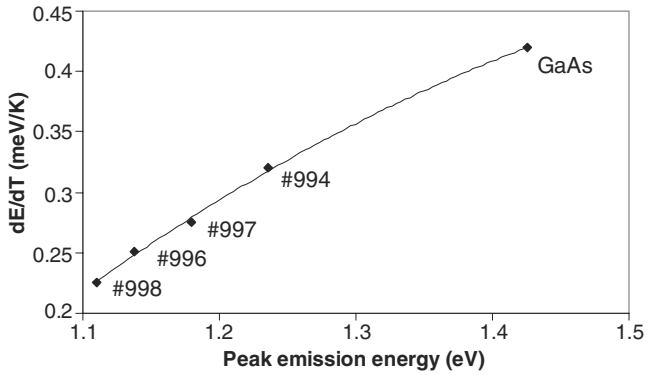

Figure 16. Linear region temperature dependence versus peak RT emission energy of GaNAs samples.

extended E_{M} band increases with nitrogen incorporation. Hence the E_{-} band becomes less like E_{M} and increasingly like the temperature-insensitive localized state [51]. The effect of nitrogen on the linear region slope was modelled using parameters from [42]. However, this gave a poor agreement to the experimental data (figure 17 dotted curve). A much better agreement was found by switching the sign of γ (figure 17 full curve), making it positive, in agreement with [44].

For each of the GaNAs samples, sets of C_{NM} and γ values were determined that allowed modelled transitions (E_{g} (300 K)) equal to the measured RT emission. Similarly, sets were determined that give linear region slopes ($\mathrm{d}E/\mathrm{d}T$) equal to the measured gradients. Values of C_{NM} and γ (table 5) that satisfy both E_{g} (300 K) and $\mathrm{d}E/\mathrm{d}T$ were then found from the two sets of data (figure 18). With the exception of sample no. 994, all γ values were positive, confirming that the localized N level shifts down in energy with increasing N fraction as in [44]. The high C_{NM} and low γ values for sample no. 994 may be due to composition or well width estimation errors. For the other samples, we find that the parameters fall into a relatively narrow range. It is interesting to note that C_{NM} appears to decrease while γ increases with nitrogen fraction. However, the significance of this should not be given too much weight in light of the limited data.

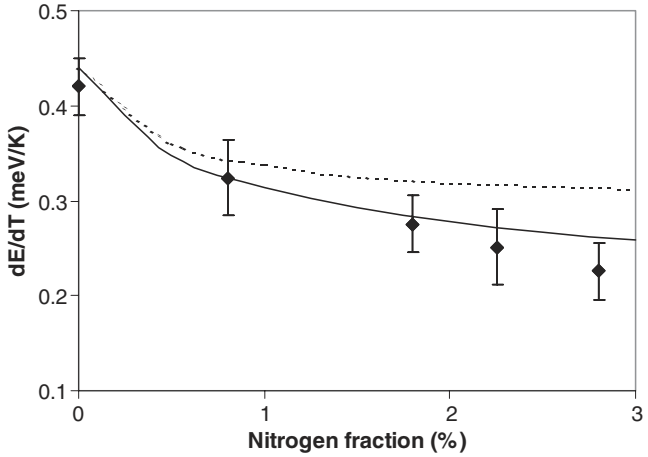

Figure 17. The effect of nitrogen on the linear region temperature dependence of GaNAs; (♦) experimental values, (- - - -) modelled dependence using $C_{\mathrm{NM}} = 2.4$ and $\gamma = -3.89$ and (——) using $C_{\mathrm{NM}} = 2.4$ and $\gamma = 3.89$.

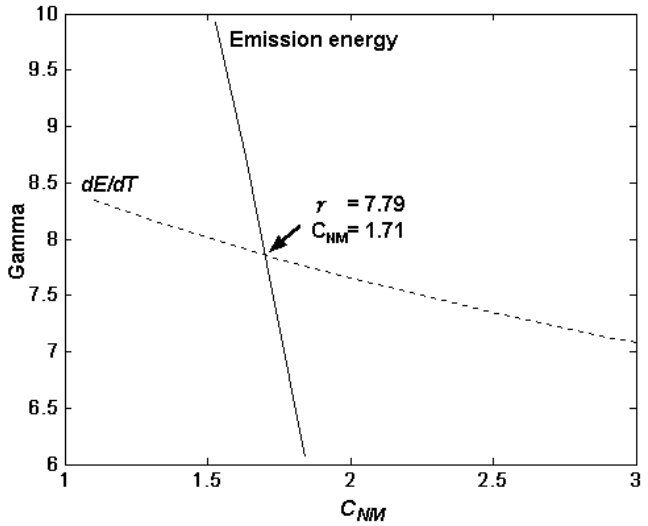

Figure 18. Modelled C_{NM} and γ values that produce the correct RT emission energy (full line) and linear region temperature dependence (broken curve) for GaNAs sample no. 998.

4.3. Non-radiative processes

The PL intensity temperature dependence of typical InGaAs and GaInNAs QWs is shown in figure 19. As with most dilute nitride samples, the GaInNAs emission intensity is significantly lower than that of the N-free InGaAs well, indicating that N incorporation gives rise to strong non-radiative recombination. While PL cannot give direct evidence of deep level traps, the poor emission efficiency, even at low temperatures, implies their presence. As_{Ga} antisite defects [78] and impurities [79–81] have been identified as deep level traps in dilute nitrides and in most cases can be effectively removed by post-growth heat treatment.

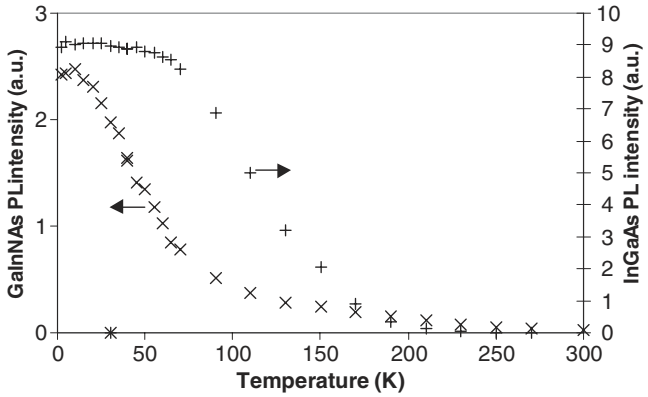

Figure 19. Peak PL intensity versus temperature for sample no. 752; (+) InGaAs, and (×) GaInNAs.

Table 5. Band anti-crossing (BAC) parameters determined using the room temperature (300 K) emission energy and temperature dependence of each GaNAs sample and GaInNAs sample no. 752.

Sample I.D.	N fraction (%)	RT emission (eV)	dE/dT (meV K^{-1})	C_{NM}	γ
994	0.8	1.23	0.32	3.85	−11.13
997	1.8	1.19	0.28	2.21	5.18
996	2.25	1.13	0.25	2.07	6.69
998	2.8	1.11	0.23	1.69	7.97
752	1.5 (20% In)	1.01	0.3	2.74	2.59

The InGaAs emission remains reasonably stable up to around 60 K, but is quenched at higher temperatures (figure 19) by thermally activated non-radiative processes. Quenching occurs in the GaInNAs at a much lower temperature (∼15 K). Assuming a Maxwell–Boltzmann carrier distribution, allows the PL intensity I at a temperature T to be described by equation (14) (where I_0 is the intensity at $T = 0$ K, τ_r and τ_∞ are the non-radiative lifetimes at a given temperature and as $T \to \infty$ and ΔE is the non-radiative trap activation energy) [82]. The activation energies of dominant loss mechanisms (table 6) can therefore be obtained from Arrhenius plots of $\ln[(I_0/I) - 1]$ versus $1/T$ (figure 20). Emission can be quenched by a number of thermally activated processes: carriers can be captured by impurity or defect traps, delocalized from efficient radiative traps and with enough energy scatter out of the QW. Most of the measured activation energies are related to shallow level traps induced by impurities and lattice defects. However, some of the larger activation energies may be associated with thermionic emission of carriers from the wells:

$$I = \frac{I_o}{1 + \frac{\tau_r}{\tau_\infty} \exp(\frac{-\Delta E}{k_B T})}. \tag{14}$$

4.4. Higher energy interband transitions

RT photomodulated reflectance (PR) measurements have been carried out on most of the samples in table 1. For lightly doped structures with low built-in or applied electric fields the PR lineshapes follow Aspnes's third derivative functional form (TDFF) [83, 84]. Fitting TDFFs

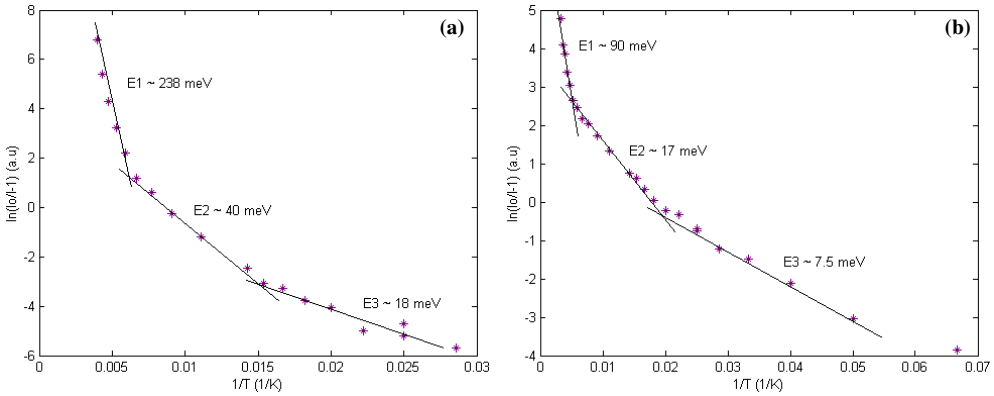

Figure 20. Arrhenius plots of the peak PL intensity between 0 K and RT for (a) InGaAs no. 752, (b) GaInNAs no. 752.

Table 6. Summary of non-radiative loss mechanism activation energies, estimated from temperature-dependent photoluminescence intensity data.

Sample no.	Quantum well	Activation $E1$ (meV)	Activation $E2$ (meV)	Activation $E3$ (meV)
752	InGaAs	238 ± 25	40 ± 5	18 ± 2
752	GaInNAs	90 ± 12	17 ± 2	7.5 ± 0.5
933	GaInNAs	53 ± 15	10.5 ± 2	7 ± 1
960	InGaAs	143 ± 15	25 ± 2	
960	GaInNAs1	23 ± 3	7 ± 1	
961	InGaAs	110 ± 10	22 ± 2	
961	GaInNAs1	55 ± 10	17.5 ± 1	7 ± 1
961	GaInNAs2	33 ± 10	6.2 ± 0.5	
983	InGaAs	90 ± 20	25 ± 2	7.5 ± 0.5
983	GaInNAs	70 ± 15	19 ± 4	6.5 ± 0.5
994	GaNAs	29 ± 4	14 ± 0.5	
996	GaNAs	28 ± 4	7 ± 1	
997	GaNAs	20 ± 4	3.5 ± 0.5	
998	GaNAs	29 ± 4	5.5 ± 0.5	
1082	InGaAs	75 ± 10	15 ± 3	
1082	GaInNAs	71 ± 5	16 ± 2	

to the PR data was carried out using the three-point method (3PM) [83] followed by least squares fitting.

The PR signal from a GaNAs QW (no. 994) is shown in figure 21 together with RT PL for comparison. The strong feature between ∼1.4 and 1.45 eV, originate from the bulk GaAs. This feature is mixed with Franz–Keldysh oscillations (FKOs) [83, 85] indicating the presence of a moderate to high electric field in the sample. It is important to note that electric fields in the sample will affect the transition selection rules. The features labelled A–D in figure 21 originate from interband transitions. The lowest energy PR feature coincides with the PL peak and similar results are found for each sample (table 7).

The interband transitions of each sample were modelled using the C_{NM} and γ parameters estimated earlier (table 5) and the measured and modelled transitions are tabulated in table 7. The lowest energy PR features match closely with the modelled e1–hh1 or e1–lh1 transitions.

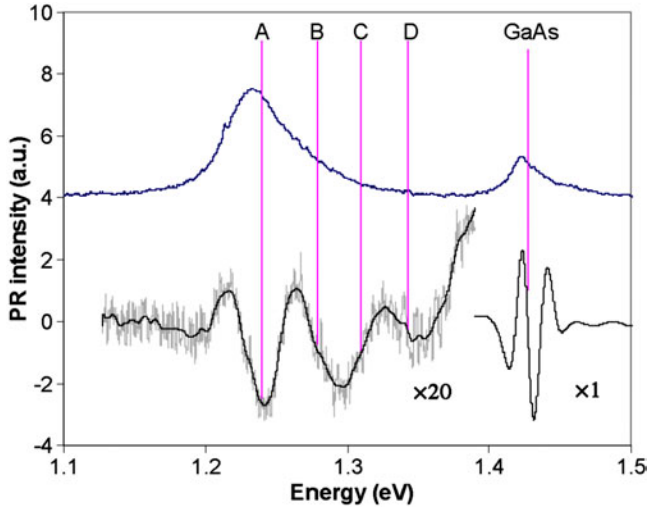

Figure 21. PR spectrum of sample no. 994 showing main spectral features and a room temperature PL spectrum for comparison.

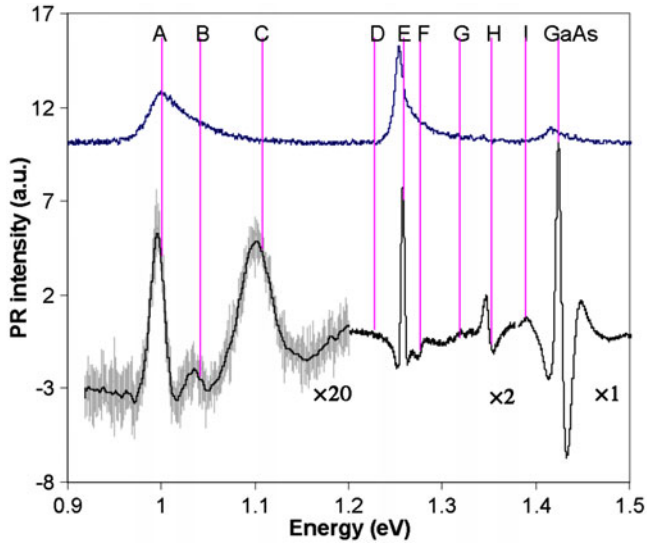

Figure 22. PR spectrum of sample no. 752, with room temperature PL spectrum for comparison.

As these are close together and the PR features are broad, resolving both is not possible; hence the signal may be a combination of both transitions. The second and third spectral features of each sample correlate closely to the e1–hh2/lh2 and e2–hh1/lh1 modelled transitions, respectively. The fourth and final transition seems to correlate with the e2–hh2/lh2 transitions for all of the samples except no. 998, in which it seems to correlate with the e3–lh1 transition.

Most of the remaining samples contain multiple QWs and the GaInNAs PR features are very broad. We will therefore only consider results from sample no. 752 for completeness. As with the GaNAs samples, strong PR features coincide with the InGaAs and GaInNAs PL peaks (figure 22). In the energy interval between 0.9 and 1.25 eV four broad PR features originating

Table 7. Photomodulated reflectance results for the GaNAs samples matched against modelled interband transition energies, plus RTe peak photoluminescence emission energies.

Sample	No. 994		No. 997		No. 996		No. 998	
N fraction	0.8%		1.8%		2.25%		2.8%	
Transition	Model (eV)	PR (eV)	Model (eV)	PR (eV)	Model (eV)	PR (eV)	Model (eV)	PR (eV)
e1–lh1	1.234	1.237	1.180		1.123	—	1.093	—
e1–hh1	1.233		1.187	1.188	1.135	1.139	1.111	1.119
e1–hh2	1.250	1.276	1.210	1.216	1.160	—	1.138	
e1–lh2	—	—	1.237		1.192	1.181	1.173	1.162
e1–hh3	—	—	—	1.253	1.199	—	1.181	—
e2–lh1	1.329	1.309	1.271		1.215	1.212	1.181	—
e2–hh1	1.329		1.278	—	1.227	—	1.199	1.205
e2–hh2	1.346	1.34	1.302	1.304	1.253	1.271	1.226	—
e2–lh2	—	—	1.329	—	1.285		1.261	—
e2–hh3	—	—	—	—	1.291	—	1.269	—
e3–lh1	—	—	1.365	—	1.331	—	1.295	1.300
e3–hh1	—	—	1.372	—	1.342	—	1.313	—
e3–hh2	—	—	1.396	—	1.368	—	1.340	—
e3–lh2	—	—	1.423	—	1.400	—	1.375	—
e3–hh3	—	—	—	—	1.407	—	1.383	—
PL Peak (eV) >	1.233		1.189		1.134		1.113	

from the GaInNAs QW are seen. Between 1.25 and 1.4 eV stronger and considerably narrower features originating from the InGaAs QW are observed. Finally, between 1.4 and 1.5 eV a strong GaAs related feature is observed. Again the transitions have been modelled using the values of C_{NM} and γ determined earlier (table 5). The measured GaInNAs transitions appear to correlate closely with the modelled transitions. However, as the PR features are broad, TDFF fitting and subsequent assignment to particular interband transitions is inaccurate. The InGaAs PR features are stronger and sharper. The first attempt at modelling these transitions used just the indium fraction as a variable. However, better agreement was found used both well width and indium fraction as variables. Increasing the well width from 90 to 100 Å and decreasing the indium fraction to 18.5% greatly improved the correlation (table 8).

4.5. Hot carrier effects

Under low excitation conditions, 'hot' carriers thermalize rapidly, reaching equilibrium with the lattice on a timescale shorter than the radiative lifetime. However, as excitation increases, a population of hot carriers is established, appearing as a high-energy exponential tail in the emission spectra. The electron–hole plasma is in thermodynamic equilibrium with the exciton gas due to collisions between the excitons and the free carriers [86]. We can therefore, deduce the free-carrier (plasma) temperature T_{e} from the exponential tail by assuming a Maxwellian distribution [87] of hot carriers given by equation (15) (where I is the PL intensity at a photon energy of $h\nu$ and k_{B} is Boltzmann's constant). Under steady state excitation, the power given to the carriers by the optical field balances that lost to the lattice. If the plasma temperature is much greater than the lattice temperature, then polar optical phonon scattering dominates the loss of carrier energy to the lattice. Under such conditions the average rate of energy lost to the lattice can be equated to the pump intensity (equation (16), where $\hbar\omega_{\mathrm{LO}}$ is the phonon

Table 8. Photomodulated reflectance results for sample no. 752 matched against modelled interband transition energies, plus RT (300 K) peak photoluminescence emission energies.

	GaInNAs transitions	Modelled 20% In, 1.5% N 90 Å QW	PR
A	e1–hh1	1.005	0.999
B	e1–hh2	1.03	1.039
	e1–hh3	1.072	
C	e1–lh1	1.084	1.104
	e2–hh1	1.114	
	e1–lh2	1.128	
	e2–hh2	1.139	
	e2–hh3	1.180	
D	e2–lh1	1.193	1.22
	e2–lh2	1.237	
	PL	1.005	

	InGaAs transition	Modelled 19% In 90 Å QW	Modelled 18.5% In 100 Å QW	PR
E	e1–hh1	1.257	1.257	1.258
F	e1–hh2	1.279	1.276	1.275
G	e1–hh3	1.314	1.306	1.311
H	e2–hh1	1.341	1.333	1.350
	e2–hh2	1.364	1.352	
I	e2–hh3	1.399	1.382	1.386
	PL	1.259		

energy and τ_{LO} is the phonon scattering time constant) [88]:

$$I \propto \exp\left(\frac{-h\nu}{k_B T_e}\right) \tag{15}$$

$$\left\langle \frac{dE}{dt} \right\rangle = \left(\frac{\hbar\omega_{LO}}{\tau_{LO}}\right) \exp\left(\frac{-\hbar\omega_{LO}}{k_B T_e}\right). \tag{16}$$

The effects of pump power on the steady state PL emission of sample no. 752 were investigated at 4.4 K. The LO phonon energy ($\hbar\omega$) was estimated by plotting the inverse carrier temperature as a function of $\ln(I)$ (figure 23), giving $\hbar\omega \sim 30.8$ and $\hbar\omega \sim 29.7$ meV for the InGaAs and GaInNAs wells, respectively. Substituting these values into equation (16) for both QWs, rearranging for τ_{LO} and taking the ratio, we find that the scattering time in the GaInNAs QW is around twice that of the InGaAs. However, this may be partly due to spectral broadening of the GaInNAs emission.

The rate of carrier cooling in InGaAs and GaInNAs QWs was investigated using low temperature (10 K) time resolved PL. Figure 24 show the carrier cooling curves for InGaAs (no. 752) and GaInNAs (no. 1087) wells. Cooling proceeds in a near linear fashion down to ∼55 K, taking around 1000 ps in the InGaAs well, but less than 200 ps in the GaInNAs well. The large population of excited carriers in the InGaAs well may inhibit cooling via hot-phonon effects and screening of long-range polar carrier–LO-phonon coupling. In contrast, cooling is enhanced in the GaInNAs by non-radiative recombination, which rapidly depletes the population of excited carriers.

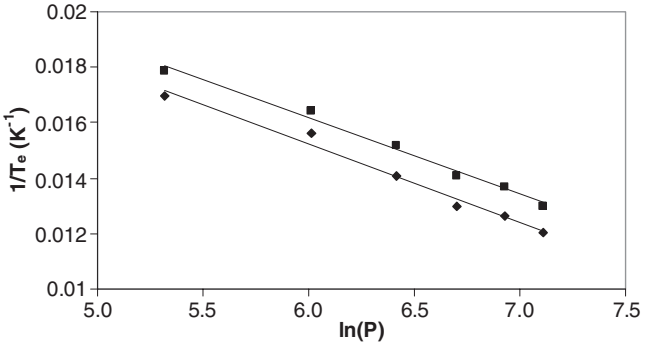

Figure 23. Logarithm of pump power versus inverse electron temperature of sample no. 752 at $T = 4.4$ K. For (■) GaInNAs and (♦) InGaAs.

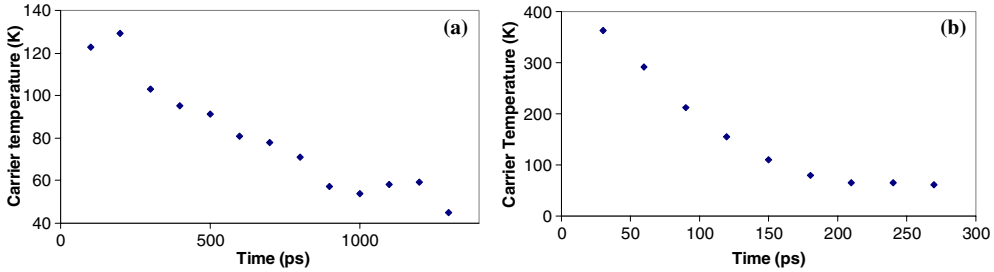

Figure 24. Temporal evolution of carrier temperature in (a) the InGaAs QW of sample no. 752 and (b) the GaInNAs QW of sample no. 1087b at 10 K with 5 mW pumping.

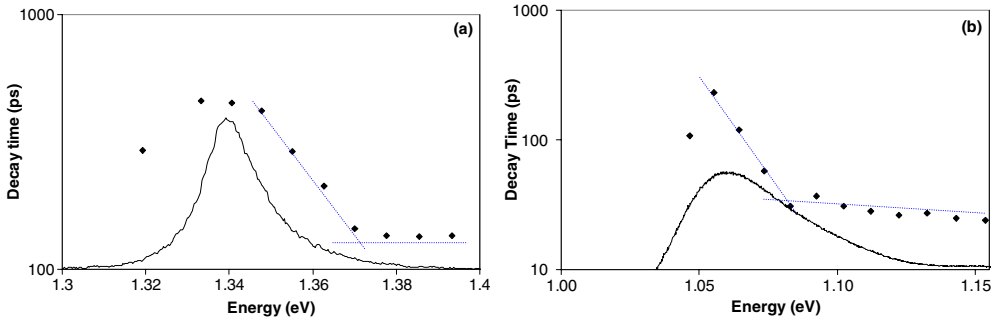

Figure 25. Semi-log plots of emission decay times versus energy at 10 K with 5 mW pump power for sample no. 752: (a) InGaAs and (b) GaInNAs. Time-integrated emission spectra are overlayed.

4.6. Decay rates

The spectral emission kinetics from both InGaAs and GaInNAs samples were found to have the longest decay times at energies close to the PL peak (figure 25). At higher energies the emission decay time decreases; dropping off rapidly at first and then gradually. The energy (E_t) at which the transition between fast and slow decay occurs is found to increase with excitation intensity (figure 26). In an ideal QW under low intensity excitation, E_t corresponds to the LO-phonon limit ($E_g + \hbar\omega_{LO}$). Carriers with energies greater than $E_g + \hbar\omega_{LO}$ can

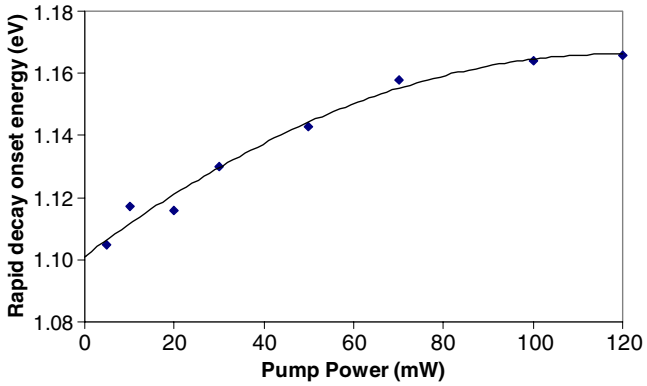

Figure 26. Plot of fast decay onset energy versus PL pump power for GaInNAs emission from sample no. 752 at 10 K.

cool rapidly via LO-phonon scattering, while those with less cool via slower acoustic-phonon scattering [89]. However, as excitation intensity increases, cooling via LO-phonon scattering is inhibited by hot-phonon and screening effects, leading to the observed shift of E_t. From the low pump intensity InGaAs results (figure 25(a)), E_t is ∼31 meV above the PL peak, which is close to the LO-phonon energy determined using steady state PL.

Similar analysis of the GaInNAs decay times could be carried out. However, the localization invalidates the interpretation. In the presence of localized states the observed low energy dependences of decay times is largely due to carrier capture into these states [90]. For localized excitonic states the translational symmetry parallel to the well plane is broken, leading to the violation of the k-selection rule $k_{ex} \approx k_{photon}$ [91]. Hence all localized states can contribute to radiative recombination, yielding relatively short radiative lifetimes [92]. There remains a finite rate at which excitons become delocalized before recombining, hence shallow states tend to have a much shorter radiative lifetime than deep states. Free excitons must obey the k-selection rules, which should lead to considerably longer lifetimes. However, if strong non-radiative processes compete with the radiative recombination then the population of free excitons is rapidly depleted, leading to the observed short lifetimes.

5. Conclusions

Dilute nitrides are potentially of great importance as a narrow bandgap material for future photonics and electronic devices. These novel materials potentially offer huge advantages over conventional narrow gap materials, allowing improved device efficiency, reduced fabrication costs, device enhancements and integration of photonic and electronic devices on a single chip.

In this work we have developed a model to calculate dilute nitride QW interband transition energies without the need for computationally demanding calculations. Modelled results were shown to be in good agreement with published $\boldsymbol{k} \cdot \boldsymbol{p}$ interband transitions. The temperature-dependent behaviour of interband transitions was modelled and compared to experimental results. The addition of nitrogen is shown to induce strong carrier localization and non-radiative recombination in dilute nitride QWs. Both effects are believed to be due to the high miscibility gap between arsenides and nitrides, which results in defect incorporation during growth. However, work by other groups indicates that these problems can be overcome by optimizing growth and post-growth heat treatment. We have investigated the effects of nitrogen

on phonon-assisted carrier cooling using steady state and time resolved photoluminescence. The incorporation of small fractions of nitrogen does not appear to have a significant effect on the LO-phonon energy. However, it leads to a significant increase in the apparent cooling rate, which is believed to result from strong non-radiative recombination.

Acknowledgments

We are grateful to H Carrère, A Arnoult, E Bedel and C Fontaine (from LAAS–CNRS, Toulouse, France) for growing the samples, S Mazzucato, D Alexandropoulos and M J Adams (from the University of Essex, UK) for useful discussions of the model and experimental results, X Marie and M Senes (from INSA–CNRS, Toulouse, France) for use of their time resolved PL set-up and assistance in running it, P Chalker and S Thomas (University of Liverpool, UK) for TEM work and EPSRC for funding this work.

References

[1] Refi J J 1999 *Bell Lab. Tech. J.* **4** 246
[2] Nouchi P, de Montmorillon L A, Sillard P, Bertaina A and Guenot P 2003 *C. R. Physique* **4** 29
[3] Schneider H C, Fischer A J, Chow W W and Klem J F 2001 *Appl. Phys. Lett.* **78** 3391
[4] Kawaguchi M, Miyamoto T, Gouardes E, Schlenker D, Kondo T, Koyama F and Iga K 2001 *Japan. J. Appl. Phys.* **40** L744
[5] Ramakrishnan A, Steinle G, Supper D, Degen C and Ebbinghaus G 2002 *Electron. Lett.* **38** 322
[6] Heroux J B, Yang X and Wang W I 1999 *Appl. Phys. Lett.* **75** 2716
[7] Kinsey G S, Gotthold D W, Holmes A L Jr and Campbell J C 2000 *Appl. Phys. Lett.* **77** 1543
[8] Kato T, Mizuno Y, Hirotani M, Saka T and Horinaka H 2001 *J. Appl. Phys.* **89** 2907
[9] Bouche N, Dupuy C, Meriadec C, Streubel K, Landrreau J, Manin L and Raj R 1998 *Appl. Phys. Lett.* **73** 2718
[10] Sato S and Satoh S 1999 *Japan. J. Appl. Phys.* **38** L990
[11] Kondow M, Kitatani T, Nakatsuka S, Larson M, Nakahara K, Yazawa Y and Okai M 1997 *IEEE J. Sel. Top. Quantum Electron.* **3** 719
[12] Dudley J J, Babic D I, Mirin R, Yang L, Miller B I, Ram R J, Reynolds T, Hu E L and Bowers J E 1994 *Appl. Phys. Lett.* **64** 1463
[13] Babic B I, Streubel K, Mirin R P, Margalit M N, Hu E L, Bowers J E, Mars D E, Yang L and Carey K 1995 *IEEE Photon. Technol. Lett.* **7** 1225
[14] Weyers M, Sato M and Ando H 1992 *Japan. J. Appl. Phys.* **31** L853
[15] Balkan N 2003 *Dilute Nitride-Arsenide-Materials for Innovative Technologies* FP6 NoE Proposal. Ref No. FP6-511321 IST-2002-2.3.2.2, October 2003 (submitted)
[16] Kurtz S R, Allerman A A, Jones E D, Gee J M, Banas J J and Hammons B E 1999 *Appl. Phys. Lett.* **74** 729
[17] Geisz J F and Friedman D J 2002 *Semicond. Sci. Technol.* **17** 769
[18] Balcioglu A, Ahrenkiel R K and Friedman D J 2000 *Appl. Phys. Lett.* **76** 2397
[19] Jalili Y S, Stavrinou P N, Roberts J S and Parry G 2002 *Electron. Lett.* **38** 343
[20] Chang P C, Baca A G, Li N Y, Sharps P R, Hou H Q, Laroche J R and Ren F 2000 *Appl. Phys. Lett.* **76** 2788
[21] Chang P C, Baca A G, Li N Y, Xie M, Hou H Q and Armour E 2000 *Appl. Phys. Lett.* **76** 2262
[22] Li N Y, Chang P C, Baca A G, Xie X M, Sharp P R and Hou H Q 2000 *Electron. Lett.* **36** 81
[23] Livshits D A, Egorov A Yu and Riechert H 2000 *Electron. Lett.* **36** 1381
[24] Tansu N and Mawst L J 2002 *IEEE Photon. Techol. Lett.* **14** 444
[25] Kawaguchi M, Miyamoto T, Gouardes E, Schlenker D, Kondo T, Koyama F and Iga K 2001 *Japan. J. Appl. Phys.* **40** L744
[26] Egorov A Yu, Bernklau D, Livshits D, Ustinov V, Alferov Zh I and Riechert H 1999 *Electron. Lett.* **35** 1643
[27] Choquette K D, Klem J F, Fischer A J, Blum O, Allerman A A, Fritz I J, Kurtz S R, Breiland W G, Sieg R, Geib K M, Scott J W and Naone R L 2000 *Electron. Lett.* **36** 1388
[28] Fischer M, Reinhardt M and Forchel A 2000 *Electron. Lett.* **36** 1208
[29] Fischer M O, Reinhardt M and Forchel A 2001 *IEEE J. Sel. Top. Quantum Electron.* **7** 149
[30] Shan W, Walukiewiez W, Ager J W, Haller E E, Geisz J F, Friedman D J, Olson J M and Kurtz S R 1999 *Phys. Rev. Lett.* **82** 1221
[31] Alexandropoulos D and Adams M J 2003 *IEE Proc. Optoelectron.* **150** 105

[32] Van de Walle C G 1989 *Phys. Rev.* B **39** 1871
[33] Chuang S L 1995 *Physics of Optoelectronic Devices* (New York: Wiley)
[34] Vurgaftman I, Meyer J R and Ram-Mohan L R 2001 *J. Appl. Phys.* **89** 5815
[35] Sakai S, Ueta Y and Terauchi Y 1993 *Japan. J. Appl. Phys.* **32** 4413
[36] Kitatani T, Kondow M, Kikawa T, Yazawa Y, Okai M and Uomi K 1999 *Japan. J. Appl. Phys.* **38** 5003
[37] Sun B Q, Jiang D S, Luo X D, Xu Z Y, Pan Z, Li L H and Wu R H 2000 *Appl. Phys. Lett.* **76** 2862
[38] Bellaiche L, Wei S H and Zunger A 1997 *Appl. Phys. Lett.* **70** 3558
[39] O'Reilly E P and Lindsay A 1999 *Phys. Status Solidi* b **216** 131
[40] Krispin P, Spruytte S G, Harris J S and Ploog K H 2000 *J. Appl. Phys.* **88** 4153
[41] Buyanova I A, Pozina G, Hai P N, Chen W M, Xin H P and Tu C W 2001 *Phys. Rev.* B **63** 033303
[42] Klar P J, Gruning H, Heimbrodt W, Koch J, Stolz W, Vicente P M A, Kamal Saadi A M, Lindsay A and O'Reilly E P 2001 *Phys. Status Solidi* b **223** 163
[43] Zhang Y, Mascarenhas A, Xin H P and Tu C W 2000 *Phys. Rev.* B **61** 7479
[44] Lindsay A and O'Reilly E P 1999 *Solid State Commun.* **112** 443
[45] Klar P J, Gruning H, Heimbrodt W, Koch J, Hohnsdorf F, Stolz W, Vicente P M A and Camassel J 2000 *Appl. Phys. Lett.* **76** 3439
[46] Makita Y, Ijuin H and Gonda S 1976 *Appl. Phys. Lett.* **28** 287
[47] Hjalmarson H P, Vogl P, Wolford D J and Dow J D 1980 *Phys. Rev. Lett.* **44** 810
[48] Chappell T I 1979 *IEEE Trans. Electron Devices* **26** 1091
[49] Shan W, Walukiewicz W, Yu K M, Ager J W III, Haller E E, Geisz J F, Friedman D J, Olson J M, Kurtz S R, Xin H P and Tu C W 2001 *Phys. Status Solidi* b **223** 75
[50] Larson M C, Kondow M, Kitatani T, Yazawa Y and Okai M 1997 *Electron. Lett.* **33** 959
[51] Suemune I, Uesugi K and Walukiewicz W 2000 *Appl. Phys. Lett.* **77** 3021
[52] Perline P, Subramanya S G, Mars D E, Kruger J, Shapiro N A, Siegle H and Weber E R 1998 *Appl. Phys. Lett.* **73** 3703
[53] Uesugi K, Suemune I, Hasegawa T, Akutagawa T and Nakamura T 2000 *Appl. Phys. Lett.* **76** 1285
[54] Potter R J, Balkan N, Marie X, Carrere H, Bedel E and Lacoste G 2001 *Phys. Status Solidi* a **187** 623
[55] Varshni Y P 1967 *Physica* **34** 149
[56] Passler R 1999 *Phys. Status Solidi* b **216** 975
[57] Perlin P, Wisniewski P, Skierbiszewski C, Suski T, Kaminska E, Subramanya S G, Weber E R, Mars D E and Walukiewicz W 2000 *Appl. Phys. Lett.* **76** 1279
[58] Skierbiszewski C, Perlin P, Wisniewski P, Suski T, Walukiewicz W, Shan W, Ager J W III, Haller E E, Geisz J F, Friedman D J, Olson J M and Kurtz S R 1999 *Phys. Status Solidi* b **216** 135
[59] Klar P J, Gruning H, Koch J, Schafer S, Volz K, Stolz W, Heimbrodt W, Kamal Saadi A M, Lindsay A and O'Reilly E P 2001 *Phys. Rev.* B **64** 121203(R)
[60] Kurtz S, Webb J, Gedvilas L, Friedman D, Geisz J, Olson J, King R, Joslin D and Karam N 2001 *Appl. Phys. Lett.* **78** 748
[61] Kim K and Zunger A 2001 *Phys. Rev. Lett.* **86** 2609
[62] Buyanova I A, Chen W M, Pozina G, Bergman J P, Monemar B, Xin H P and Tu C W 1999 *Appl. Phys. Lett.* **75** 501
[63] Gokhale M R, Wei J, Wang H and Forrest S R 1999 *Appl. Phys. Lett.* **74** 1287
[64] Pan Z, Li L H, Zhang W, Lin Y W, Wu R H and Ge W 2000 *Appl. Phys. Lett.* **77** 1280
[65] Yang X, Jurkovic M J, Heroux J B and Wang W I 1999 *Appl. Phys. Lett.* **75** 178
[66] Mair R A, Lin J Y, Jiang H X, Jones E D, Allerman A A and Kurtz S R 2000 *Appl. Phys. Lett.* **76** 188
[67] Pan Z, Miyamoto T, Schlenker D, Sato S, Koyama F and Iga K 1998 *J. Appl. Phys.* **84** 6409
[68] Oueslati M, Zouaghi M, Pistol M E, Samuelson L, Grimmeiss H G and Balkenski M 1985 *Phys. Rev.* B **32** 8220
[69] Cho Y H, Gainer G H, Fischer A J, Song J J, Keller S, Mishra U K and DenBaars S P 1998 *Appl. Phys. Lett.* **73** 1370
[70] Moon Y T, Kim D J, Park J S, Oh J T, Lee J M, Ok Y W, Kim H and Park S J 2001 *Appl. Phys. Lett.* **79** 599
[71] Naranjo F B, Sanchez-Garcia M A, Calle F, Calleja E, Jenichen B and Ploog K H 2002 *Appl. Phys. Lett.* **80** 231
[72] Cho Y H, Gainer G H, Lam J B, Song J J, Yang W and Jhe W 2000 *MRS Internet J. Nitride Semicond. Res.* **5** U685
[73] Kaschner A, Luttgert T, Born H, Hoffmann A, Egorov A Yu and Riechert H 2001 *Appl. Phys. Lett.* **78** 1391
[74] Grenouillet L, Bru-Chevallier C, Guillot G, Gilet P, Duvaut P, Vannuffel C, Million A and Chenevas-Paule A 2000 *Appl. Phys. Lett.* **76** 2241
[75] Pinault M A and Tournie E 2001 *Appl. Phys. Lett.* **78** 1562
[76] Francoeur S, Nikishin S A, Jin C, Qiu Y and Tempkin H 1999 *Appl. Phys. Lett.* **75** 1538
[77] Potter R J, Balkan N, Marie X, Carrere H and Bedel E 2001 *Phys. Status Solidi* a **187** 623

[78] Thinh N Q, Buyanova I A, Hai P N, Chen W M, Xin H P and Tu C W 2001 *Phys. Rev.* B **63** 033203
[79] Kwon D, Kaplar R J, Ringel S A, Allerman A A, Kurtz S R and Jones E D 1999 *Appl. Phys. Lett.* **74** 2830
[80] Krispin P, Spruytte S G, Harris J S and Ploog K H 2001 *J. Appl. Phys.* **89** 6294
[81] Kaplar R J, Arehart A R, Ringel S A, Allerman A A, Sieg R M and Kurtz S R 2001 *J. Appl. Phys.* **90** 3405
[82] Karachevtseva M V, Ignat'ev A S, Mokerov V G, Nemtsev G Z, Strakhov V A and Yaremenko N G 1994 *Semiconductors* **28** 691
[83] Aspnes D E 1973 *Surf. Sci.* **37** 418
[84] Glembocki O J and Shanabrook B V 1966 *Semiconductors and Semimetals* vol 36, ed R K Willardson and A C Beer (New York: Academic) chapter 4, p 221
[85] Hughes P J, Weiss B L and Hosea T J C 1995 *J. Appl. Phys.* **77** 6472
[86] Robart D, Marie X, Baylac B, Amand T, Brousseau M, Bacquet G, Debart G, Planel R and Gerard J M 1995 *Solid State Commun.* **95** 287
[87] Shah J 1992 *Hot Carriers in Semiconductor Nanostructures: Physics and Applications* ed J Shah (New York: Academic) p 279
[88] Conwell E M 1967 *High Field Transport in Semiconductors* (New York: Academic)
[89] Ryan J F 1985 *Physica* B and C **134** 403
[90] Mair R A, Lin J Y, Jiang H X, Jones E D, Allerman A A and Kurtz S R 2000 *Appl. Phys. Lett.* **76** 188
[91] Christen J, Krahl M and Bimberg D 1990 *Superlatt. Microstruct.* **7** 1
[92] Marie X, Lephay F, Amand T, Barrau J, Voillot F and Brousseau M 1991 *Superlatt. Microstruct.* **10** 415